

Monolayer control of spin-charge conversion in van der Waals heterostructures

Khasan Abdukayumov,¹ Oliver Paull,² Martin Mičica,³ Fatima Ibrahim,¹ Libor Vojáček,¹ Adrien Wright,³ Sylvain Massabeau,² Federico Mazzola,⁴ Vincent Polewczyk,¹ Cyriack Jego,¹ Rahul Sharma,¹ Céline Vergnaud,¹ Alain Marty,¹ Isabelle Gomes de Moraes,¹ Abdelkarim Ouerghi,⁵ Hanako Okuno,⁶ Anupam Jana,⁷ Indrani Kar,⁷ Jun Fuji,⁷ Ivana Vobornik,⁷ Jing Li,⁸ Frédéric Bonell,¹ Mairbek Chshiev,^{1,9} Manuel Bibes,² Jean-Marie George,² Henri Jaffrès,² Sukhdeep Dhillon,³ and Matthieu Jamet¹

¹*Université Grenoble Alpes, CEA, CNRS,
IRIG-SPINTEC, 38000 Grenoble, France*

²*Laboratoire Albert Fert, CNRS, Thales, Université Paris-Saclay,
1 avenue Augustin Fresnel, 91767, Palaiseau France*

³*Laboratoire de Physique de l'École normale supérieure,
ENS, Université PSL, CNRS, Sorbonne Université,
Université de Paris, 24 rue Lhomond, 75005 Paris, France*

⁴*Department of Molecular Sciences and Nanosystems,
Ca'Foscari University of Venice, Venice, Italy*

⁵*Université Paris-Saclay, CNRS, Centre de Nanosciences
et de Nanotechnologies, 91120, Palaiseau, France*

⁶*Université Grenoble Alpes, CEA, IRIG-MEM, 38000 Grenoble, France*

⁷*CNR-IOM Laboratorio TASC, I-34149 Trieste, Italy*

⁸*Université Grenoble Alpes, CEA-LETI, 38000 Grenoble, France*

⁹*Institut Universitaire de France, Paris, 75231 France*

(Dated: January 7, 2025)

Abstract

The diversity of 2D materials and their van der Waals (vdW) stacking presents a fertile ground for engineering novel multifunctional materials and quantum states of matter. This permits unique opportunities to tailor the electronic properties of vdW heterostructures by the insertion of only a single 2D material layer. However, such vdW materials engineering at the atomic scale has yet to be investigated for spin-charge interconversion phenomena. Here, we report on the control of these effects at the monolayer level, where drastic increase in intensity and change in sign of THz spintronic emission are demonstrated by inserting a single layer of MoSe₂ between PtSe₂ and graphene in a fully epitaxial, large area stacked structure. By using a combination of spin and angle resolved photoemission and density functional theory to reveal the electronic and spin structures, we illustrate two different mechanisms relying on charge transfer and electronic hybridization for the formation of Rashba states, which are responsible for spin-charge conversion and hence the THz spintronic emission. These findings open new pathways to design, at the atomic scale, efficient THz spintronic emitters made of 2D materials and other spintronic devices based on spin-charge interconversion phenomena.

Introduction - The field of two-dimensional (2D) van der Waals (vdW) heterostructures has revealed a whole new world of exotic materials hosting a wide variety of physical properties [1, 2]. In 2D transition metal dichalcogenides (TMDs), spin-charge interconversion has emerged as a promising avenue for spintronics information processing and storage by virtue of their atomically thin nature and layer-dependent electronic and magnetic properties [3–5]. This is a core phenomenon in the field of spintronics, wherein a spin current can be converted into a charge current and vice versa through a number of mechanisms that are based on spin-orbit coupling [6]. This interconversion can be the result of the Rashba-Edelstein effect [7], the spin-Hall effect [8] or more recently the orbital-Hall effect [9] (both direct and inverse). The spin-Hall effect, being a bulk effect, occurs in materials where there is strong spin-orbit coupling, typically requiring particular materials with heavy elements. On the other hand, the Rashba-Edelstein effect is a surface/interface effect and can be induced artificially by introducing an interface in a system to break inversion symmetry. It opens up spin-charge interconversion to a myriad of material combinations and, more particularly, to vdW heterostructures where interfaces are atomically sharp and well defined [10, 11].

Initially, exfoliation methods from bulk samples produced the highest quality 2D monolayer samples at the expense of being limited to small areas on the order of micrometres. Similarly, for bilayer 2D heterostructures, advanced exfoliation and stacking methods have been developed *in* and *ex vacuo*. Only more recently have growth methods such as molecular beam epitaxy (MBE) and chemical vapor deposition (CVD) have produced high crystalline quality 2D materials and vdW heterostructures through the optimization of surface preparation and specific growth recipes [12–17]. Throughout this development in synthesis and heterostructure design, it has become apparent that the interface between van der Waals materials permits considerably more versatility compared to traditional epitaxy owing to the alleviated requirement of lattice matching of epilayers. With the mitigation of this requisite, additional methods to add and tune properties, such as twisted-angle bilayers [18], have become feasible. The ability to epitaxially grow 2D TMDs in a high-quality heterostructure on large area has been demonstrated by a limited number of research groups [19–25].

Here, we demonstrate the spin-charge conversion (SCC) at PtSe₂/Gr and PtSe₂/MoSe₂ interfaces grown by molecular beam epitaxy on large area, and show that the sign and amplitude of the SCC can be drastically modified by changing the adjacent material from graphene to MoSe₂ hence allowing monolayer control of SCC. It has been previously shown that the spin texture in PtSe₂ displays a helical character which evolves with the number of layers [26, 27]. To design a spintronic device based on the Rashba-induced helical spin texture of PtSe₂, accurate control over this spin texture must therefore be established. We employ spin and angle-resolved photoelectron emission spectroscopy (Spin-ARPES) and THz emission spectroscopy to probe the spin-charge conversion characteristics and reveal that inserting only a single layer of MoSe₂ between PtSe₂ and graphene induces a sign change and stronger SCC. First-principles calculations indeed demonstrate two different mechanisms at the origin of the spin texture: charge transfer at the PtSe₂/Gr interface and electronic hybridization at the PtSe₂/MoSe₂ van der Waals interface. This work shows the strength of vdW materials to fine-tune spin texture and SCC at the atomic scale in future spintronic devices thanks to well-defined interfaces.

Material growth and characterization - Bilayers of MoSe₂ and PtSe₂ were grown on a graphene/6H-SiC(0001) substrate using a custom MBE system [5, 28, 29]. Reflection high-energy electron diffraction (RHEED) was used to monitor the layer-by-layer growth *in-situ*,

displaying diffraction rods for MoSe₂ (Fig.1(a)i) and PtSe₂ (Fig.1(a)ii). We observe very thin and continuous diffraction lines showing the high crystalline quality of the vdW materials and the epitaxial relationship between MoSe₂ and PtSe₂. The layer stacking is shown in Fig.1(b)i (viewed along [100]) and Fig.1(b)ii (viewed along [110]) and depicts epitaxial 2D monolayers of PtSe₂ and MoSe₂ on graphene. The corresponding cross section transmission electron microscopy [28] image is shown in Fig.1(c) where we clearly distinguish the TMD layers and graphene.

To verify the epitaxy and single-crystalline nature of the 2D heterostructure, in-plane X-ray diffraction measurements (XRD) were performed [28]. In Fig.1(d), radial scans confirm that the [010] and [110] crystal directions for MoSe₂ and PtSe₂ are epitaxially aligned with those of graphene (*i.e.* with a twist angle of 0°). The azimuthal XRD scans in Fig.1(e) exhibit peaks separated by 60 degrees as expected for hexagonal symmetry, and demonstrate the high-quality single-crystal nature of the 2D layers.

To elucidate the spin texture of this bilayer, Spin-ARPES was used. The photoemission experiments were performed at the low-energy end-station of the Advanced Photoemission Experiment (APE) beamline, at the synchrotron radiation source Elettra [30] (Trieste). The energy and momentum resolutions were better than 12 meV and 0.02 Å⁻¹, respectively. The spin-integrated energy versus momentum spectra along the Γ -K high symmetry direction of the Brillouin zone are shown in Fig. 2(a), along with the theoretical electronic structure calculated by density functional theory-based approach (DFT, blue lines) [28]. An overall good agreement between the experimental measurements and calculations was observed and the main spectroscopic features are captured by the DFT. This includes, in agreement with previous calculations [31], a sombrero-like dispersion, with a maximum located ≈ 0.5 eV below the Fermi level. Such a sombrero-dispersion, according to our DFT calculations, is spin-split, featuring spin-momentum locking with Rashba-like physics. Therefore, the spins change sign from positive to negative values of momenta ($\pm k$). The spin-momentum locking is directly demonstrated by the Spin-ARPES measurements (see Fig.2(b-c) for selected energy-distribution curves resolved in (σ_y) which show strong signals with $+k$ and $-k$ connected by the enforcement of time-reversal symmetry in the system. We notice that the spin-splitting of the sombrero-dispersion in Fig.2(b) and (c) is not immediately resolved by Spin-ARPES, probably owing to a combination of photoemission matrix elements and

experimental resolutions. However, the band edges can be identified by using the second derivative of the spectra in Fig.2(d), allowing us to set 0.15 eV as the upper value for the expected spin-splitting. This is highlighted by plotting the predicted spin-polarized bands (blue and red lines) calculated by DFT on the same figure. To better identify the fermiology of the sombrero-dispersion, we extracted a constant energy map (Fig.2(e)) at $E_b = -0.65$ eV with the calculated spin texture. The shape reflects the hexagonal symmetry of the crystal. Remarkably, compared to individual PtSe₂ and MoSe₂ monolayers, the top of the sombrero-dispersion is closer to the Fermi level and originates from interface hybridization between PtSe₂ and MoSe₂ as discussed in the following. We theoretically found the same sombrero-dispersion for the PtSe₂/WSe₂ bilayer [28] showing the general character of this hybridization. Further by selecting properly the 2D material couple, it could be possible to create a two-dimensional electron or hole gas at the interface between two semiconducting materials (i.e. hybridized band crossing the Fermi level), which is reminiscent of 2D electron gases in LaAlO₃/SrTiO₃ interfaces. It points at the important role of orbital hybridization to create artificially metallic interfacial systems [32].

THz measurements - THz time domain spectroscopy experiments were carried out on the PtSe₂/MoSe₂ bilayer, and compared with those on 1 ML PtSe₂ epitaxially grown on graphene/SiC [28]. To perform these measurements, 3 nm of CoFeB and 4 nm of Al were deposited which naturally oxidizes into AlO_x. The sharp and high quality of the ferromagnet/TMD interface has been confirmed by Raman spectroscopy, x-ray photoemission spectroscopy (XPS) and scanning transmission electron microscopy (STEM)[5]. As schematically shown in Fig. 3(a-b), the measurements were carried out with a femtosecond excitation (centre wavelength of 800 nm (1.55 eV)) for both samples in transmission mode, generating a spin current in the CoFeB layer that is converted into an ultrafast charge current in the 2D material, emitting a THz pulse by SCC. The sample was pumped from the substrate side as it showed stronger measured THz electric field. As presented in Fig. 3(c) and (d), the bilayer PtSe₂/MoSe₂/Gr sample exhibits around 3.5 times stronger THz electric field than 1 ML of PtSe₂/Gr with opposite THz electric field polarity. To extract the magnetic contribution S_M and non-magnetic contribution S_{NM} from the THz signal S_{THz} , we use: $S_M = (S_{THz}(+B) - S_{THz}(-B))/2$ and $S_{NM} = (S_{THz}(+B) + S_{THz}(-B))/2$ [33]. The azimuthal angular dependence of the magnetic contribution S_M in Fig. 3(e) corresponds to

the SCC and shows an isotropic behavior as expected for THz spintronic emission [33]. In Fig. 3(e), for the non-magnetic contribution, S_{NM} , we find very weak angular dependence and do not recover the expected 6-fold symmetry from non-linear THz emission of 1 ML MoSe₂ owing to inversion symmetry breaking [34]. This observation emphasizes the electronic hybridization of MoSe₂ with PtSe₂, which modifies the electronic band structure and symmetries of the system.

Moreover, due to its proximity to the Fermi level and low effective mass, the sombrero-like band is likely to contribute to SCC for the THz emission thus justifying the different intensity and sign of THz emission when compared to PtSe₂/Gr as discussed further below.

DFT calculations - To understand in more details the role of MoSe₂ insertion between PtSe₂ and graphene on SCC, we have employed first-principles calculations to compare the PtSe₂/MoSe₂/Gr to the PtSe₂/Gr interface [28, 35–41]. The interaction across the interface is preliminarily described by the induced changes in the charge density shown in Fig. 4 (a) and (d) for PtSe₂/Gr and PtSe₂/MoSe₂/Gr heterostructures, respectively. From the planar averages [28], the estimated charge transfer is $0.04e$ from graphene to PtSe₂ while a less significant $0.007e$ is transferred from MoSe₂ to PtSe₂. This implies that the dipoles at both interfaces have the same direction pointing towards the PtSe₂ layer with a smaller magnitude at the PtSe₂/MoSe₂ interface. Therefore, the change of SCC sign upon MoSe₂ insertion cannot be explained in a simple picture of reversing the interface dipole. However, it can be clearly seen in Fig. 4(d) that the overlap of the charge clouds is more significant at this interface implying a strong hybridization between the PtSe₂ and MoSe₂ layers. In conclusion, the interaction mechanism in PtSe₂/MoSe₂/Gr governed by hybridization is different from PtSe₂/Gr that is driven by charge transfer. The hybridization strength is discerned from the calculated band structures in Fig. 4 (b) and (e) for PtSe₂/Gr and PtSe₂/MoSe₂/Gr, respectively. A weak hybridization is reflected through the preserved band structure features of both pristine graphene and PtSe₂, while the modified band features reveal the stronger hybridization between PtSe₂ and MoSe₂. Importantly, the inversion symmetry breaking imposed by the interface in both systems induces a Rashba splitting of the bands owing to the presence of spin-orbit interaction. This is depicted from the expected values of the spins projected on the y -direction $\langle\sigma^y\rangle$ along the $-\text{K} \rightarrow \Gamma \rightarrow \text{K}$ path in the Brillouin zone. To compare the SCC efficiency in PtSe₂/MoSe₂/Gr to PtSe₂/Gr, we proceed by fitting

the calculated band structures to a free-electron model as described in the Supplemental Material [28, 42]. This permits to quantify the SCC efficiency characterized by the tensor κ_{yx} integrated along the k_x path [42]:

$$\kappa_{yx} \propto \int_{-k_x^{lim}}^{+k_x^{lim}} \langle \sigma^y \rangle v_g^x 2\pi |k| dk \quad (1)$$

where k_x^{lim} was chosen as $0.6 \times |\Gamma K|$ length, $v_g^x = \partial E / \partial k_x$ is the group velocity along x and $|k|$ accounts for the growing Fermi line circumference with the distance from the Γ point. Fig. 4 (c) and (f) show the cumulative κ_{yx} values in arbitrary units arising from the highest Rashba-split valence bands in PtSe₂/Gr and PtSe₂/MoSe₂/Gr, respectively. We only focus here on the valence bands since the conduction bands show almost no spin polarization in both systems. From the energy profile of κ_{yx} , for the PtSe₂/Gr case the highest valence band has a weak positive contribution which is competing with the negative one of the lower two bands. On the other hand, the highest occupied band (sombbrero hat) featuring the strong PtSe₂/MoSe₂ hybridization acquires a large Rashba splitting that drives the overall SCC to large positive values. This cannot be compensated by the negative contribution from the lower band. A detailed description of the bands' contribution to the SCC sign is provided in the Supplemental Material [28]. Since the exact position of the Fermi level is unknown and might be different for PtSe₂/Gr and PtSe₂/MoSe₂/Gr, we assume that it is positioned at zero energy in the band diagrams of Fig. 4(b) and (e). The photon energy of the excitation laser (≈ 1.55 eV) is indicated as an orange arrow in Fig. 4(b) and (e) and sets the deepest valence bands involved in SCC. Considering the narrow energy windows close to the photon energy in orange in Fig. 4(b) and (e), we theoretically obtain $-150 \leq \kappa_{yx} \leq 0$ for PtSe₂/Gr and $\kappa_{yx} \approx 600$ for PtSe₂/MoSe₂/Gr which is in good qualitative agreement with experimental results in terms of SCC sign and relative intensity.

Conclusion - In conclusion, we demonstrate the growth of single crystalline van der Waals heterostructures over large areas using MBE and study SCC through THz spintronic emission. We show that inserting a single layer of MoSe₂ between graphene and PtSe₂ drastically changed the resulting SCC intensity and sign. DFT calculations supported by Spin-ARPES measurements pointed at two different mechanisms for the formation of the Rashba states responsible for SCC. In PtSe₂/Gr, the spin texture comes from charge transfer between PtSe₂ and graphene while it originates from the strong electronic hybridization between the two

TMD layers in PtSe₂/MoSe₂/Gr as a consequence of the epitaxial stack. The calculation of SCC based on the band structure agrees well with the spintronic THz emission. This work demonstrates the great interest of 2D materials and their vdW heterostructures to fine-tune spin textures and SCC at the atomic scale thanks to well-defined vdW interfaces. They thus constitute promising systems to design compact and efficient spintronic THz emitters or other spintronic devices involving SCC.

ACKNOWLEDGEMENTS

The authors acknowledge the support from the European Union's Horizon 2020 research and innovation Programme under grant agreements No 881603 (Graphene Flagship), No 964735 (FET-OPEN EXTREME-IR) and No 800945-NUMERICS-H2020-MSCA-COFUND-2017. O.P. and M.B. acknowledge financial support from ERC AdG "FRESCO" (#833973). Spin-tec was supported by the FLAG-ERA grant MNEMOSYN. The French National Research Agency (ANR) is acknowledged for its support through the ANR-18-CE24-0007 MAGIC-VALLEY, ANR-20-CE24-0015 ELMAX and ESR/EQUIPEX+ ANR-21-ESRE-0025 2D-MAG projects. The LANEF framework (No. ANR-10-LABX-0051) is acknowledged for its support with mutualized infrastructure. Part of the calculations were performed on computational resources provided by GENCI-IDRIS (Grant 2024-A0150912036).

-
- [1] A. K. Geim and I. V. Grigorieva, Van der Waals heterostructures, *Nature* **499**, 419 (2013).
 - [2] E. Y. Andrei, D. K. Efetov, P. Jarillo-Herrero, A. H. MacDonald, K. F. Mak, T. Senthil, E. Tutuc, A. Yazdani, and A. F. Young, The marvels of moiré materials, *Nature Review Materials* **6**, 201 (2021).
 - [3] R. Galceran, B. Tian, J. Li, F. Bonell, M. Jamet, C. Vergnaud, A. Marty, J. H. García, J. F. Sierra, M. V. Costache, S. Roche, S. O. Valenzuela, A. Manchon, X. Zhang, and U. Schwingenschlögl, Control of spin-charge conversion in van der Waals heterostructures, *APL Materials* **9**, 100901 (2021).
 - [4] J. F. Sierra, J. Fabian, R. K. Kawakami, S. Roche, and S. O. Valenzuela, Van der Waals heterostructures for spintronics and opto-spintronics, *Nature Nanotechnology* **16**, 856 (2021).

- [5] K. Abdukayumov, M. Mičica, F. Ibrahim, L. Vojáček, C. Vergnaud, A. Marty, J.-Y. Veullen, P. Mallet, I. G. de Moraes, D. Dosenovic, S. Gambarelli, V. Maurel, A. Wright, J. Tignon, J. Mangeney, A. Ouerghi, V. Renard, F. Mesple, J. Li, F. Bonell, H. Okuno, M. Chshiev, J.-M. George, H. Jaffrès, S. Dhillon, and M. Jamet, Atomic-layer controlled transition from inverse rashba–edelstein effect to inverse spin hall effect in 2d ptse₂ probed by thz spintronic emission, *Advanced Materials* , 2304243 (2024).
- [6] J.-C. Rojas-Sánchez and A. Fert, Compared efficiencies of conversions between charge and spin current by spin-orbit interactions in two- and three-dimensional systems, *Phys. Rev. Appl.* **11**, 054049 (2019).
- [7] J. C. R. Sánchez, L. Vila, G. Desfonds, S. Gambarelli, J. P. Attané, J. M. D. Teresa, C. Magén, and A. Fert, Spin-to-charge conversion using rashba coupling at the interface between non-magnetic materials, *Nature Communications* **4**, 2944.
- [8] S. O. Valenzuela and M. Tinkham, Direct electronic measurement of the spin hall effect, *Nature* **442**, 176 (2006).
- [9] D. Go, D. Jo, C. Kim, and H.-W. Lee, Intrinsic spin and orbital hall effects from orbital texture, *Phys. Rev. Lett.* **121**, 086602 (2018).
- [10] H. Yang, S. O. Valenzuela, M. Chshiev, S. Couet, B. Dieny, B. Dlubak, A. Fert, K. Garello, M. Jamet, D.-E. Jeong, K. Lee, K. Lee, M.-B. Martin, G. S. Kar, P. Sénéor, H.-J. Shin, and S. Roche, Two-dimensional materials prospects for non-volatile spintronic memories, *Nature* **606**, 663 (2022).
- [11] Q. H. Wang, A. Bedoya-Pinto, M. Blei, A. H. Dismukes, A. Hamo, S. Jenkins, M. Koperski, Y. Liu, Q.-C. Sun, E. J. Telford, H. H. Kim, M. Augustin, U. Vool, J.-X. Yin, L. H. Li, A. Falin, C. R. Dean, F. Casanova, R. F. L. Evans, M. Chshiev, A. Mishchenko, C. Petrovic, R. He, L. Zhao, A. W. Tsen, B. D. Gerardot, M. Brotons-Gisbert, Z. Guguchia, X. Roy, S. Tongay, Z. Wang, M. Z. Hasan, J. Wrachtrup, A. Yacoby, A. Fert, S. Parkin, K. S. Novoselov, P. Dai, L. Balicas, and E. J. G. Santos, The magnetic genome of two-dimensional van der waals materials, *ACS Nano* **16**, 6960 (2022).
- [12] Z. Cai, B. Liu, X. Zou, and H.-M. Cheng, Chemical vapor deposition growth and applications of two-dimensional materials and their heterostructures, *Chemical Reviews* **118**, 6091 (2018).
- [13] M. T. Dau, M. Gay, D. Di Felice, C. Vergnaud, A. Marty, C. Beigné, G. Renaud, O. Renault, P. Mallet, T. Le Quang, J.-Y. Veullen, L. Huder, V. T. Renard, C. Chapelier, G. Zamborlini,

- M. Jugovac, V. Feyer, Y. J. Dappe, P. Pochet, and M. Jamet, Beyond van der Waals Interaction: The Case of MoSe₂ Epitaxially Grown on Few-Layer Graphene, *ACS Nano* **12**, 2319 (2018).
- [14] E. Xenogiannopoulou, P. Tsipas, K. E. Aretouli, D. Tsoutsou, S. A. Giamini, C. Bazioti, G. P. Dimitrakopoulos, P. Komninou, S. Brems, C. Huyghebaert, I. P. Radu, and A. Dimoulas, High-quality, large-area mose₂ and mose₂/bi₂se₃ heterostructures on aln(0001)/si(111) substrates by molecular beam epitaxy, *Nanoscale* **7**, 7896 (2015).
- [15] A. Rajan, K. Underwood, F. Mazzola, and P. D. C. King, Morphology control of epitaxial monolayer transition metal dichalcogenides, *Phys. Rev. Mater.* **4**, 014003 (2020).
- [16] C. Vergnaud, M.-T. Dau, B. Grévin, C. Licitra, A. Marty, H. Okuno, and M. Jamet, New approach for the molecular beam epitaxy growth of scalable WSe₂ monolayers, *Nanotechnology* **31**, 255602 (2020).
- [17] M. T. Dau, C. Vergnaud, A. Marty, C. Beigné, S. Gambarelli, V. Maurel, T. Journot, B. Hyot, T. Guillet, B. Grévin, H. Okuno, and M. Jamet, The valley nernst effect in wse₂, *Nature Communications* **10**, 5796 (2019).
- [18] S. Carr, D. Massatt, S. Fang, P. Cazeaux, M. Luskin, and E. Kaxiras, Twistronics: Manipulating the electronic properties of two-dimensional layered structures through their twist angle, *Phys. Rev. B* **95**, 075420 (2017).
- [19] Y. Gong, J. Lin, X. Wang, G. Shi, S. Lei, Z. Lin, X. Zou, G. Ye, R. Vajtai, B. I. Yakobson, H. Terrones, M. Terrones, B. K. Tay, J. Lou, S. T. Pantelides, Z. Liu, W. Zhou, and P. M. Ajayan, Vertical and in-plane heterostructures from WS₂/MoS₂ monolayers, *Nature Mater* **13**, 1135 (2014).
- [20] Q. Guillet, L. Vojáček, D. Dosenovic, F. Ibrahim, H. Boukari, J. Li, F. Choueikani, P. Ohresser, A. Ouerghi, F. Mesple, V. Renard, J.-F. m. c. Jacquot, D. Jalabert, H. Okuno, M. Chshiev, C. Vergnaud, F. Bonell, A. Marty, and M. Jamet, Epitaxial van der waals heterostructures of cr₂te₃ on two-dimensional materials, *Phys. Rev. Mater.* **7**, 054005 (2023).
- [21] L. Khalil, D. Pierucci, E. Velez-Fort, J. Avila, C. Vergnaud, P. Dudin, F. Oehler, J. Chaste, M. Jamet, E. Lhuillier, M. Pala, and A. Ouerghi, Hybridization and localized flat band in the WSe₂/MoSe₂ heterobilayer, *Nanotechnology* **34**, 045702 (2022).
- [22] T. Guillet, R. Galceran, J. F. Sierra, F. J. Belarre, B. Ballesteros, M. V. Costache, D. Dosenovic, H. Okuno, A. Marty, M. Jamet, F. Bonell, and S. O. Valenzuela, Spin–Orbit Torques

- and Magnetization Switching in $(\text{Bi,Sb})_2\text{Te}_3/\text{Fe}_3\text{GeTe}_2$ Heterostructures Grown by Molecular Beam Epitaxy, *Nano Letters* **24**, 822 (2024).
- [23] K. E. Aretouli, D. Tsoutsou, P. Tsipas, J. Marquez-Velasco, S. AminaIragia Giamini, N. Kelaïdis, V. Psycharis, and A. Dimoulas, Epitaxial 2D $\text{SnSe}_2/2\text{D WSe}_2$ van der Waals Heterostructures, *ACS Applied Materials & Interfaces* **8**, 23222 (2016).
- [24] S. Kezilebieke, M. N. Huda, P. Dreher, I. Manninen, Y. Zhou, J. Sainio, R. Mansell, M. M. Ugeda, S. van Dijken, H.-P. Komsa, and P. Liljeroth, Electronic and magnetic characterization of epitaxial VSe_2 monolayers on superconducting NbSe_2 , *Communications Physics* **3**, 116 (2020).
- [25] A. Ohtake and Y. Sakuma, Two-Dimensional $\text{WSe}_2/\text{MoSe}_2$ Heterostructures Grown by Molecular-Beam Epitaxy, *The Journal of Physical Chemistry C* **125**, 11257 (2021).
- [26] M. Yan, E. Wang, X. Zhou, G. Zhang, H. Zhang, K. Zhang, W. Yao, N. Lu, S. Yang, S. Wu, T. Yoshikawa, K. Miyamoto, T. Okuda, Y. Wu, P. Yu, W. Duan, and S. Zhou, High quality atomically thin PtSe_2 films grown by molecular beam epitaxy, *2D Mater.* **4**, 045015 (2017), number: 4.
- [27] W. Yao, E. Wang, H. Huang, K. Deng, M. Yan, K. Zhang, K. Miyamoto, T. Okuda, L. Li, Y. Wang, H. Gao, C. Liu, W. Duan, and S. Zhou, Direct observation of spin-layer locking by local Rashba effect in monolayer semiconducting PtSe_2 film, *Nat Commun* **8**, 14216 (2017).
- [28] See Supplemental Material at Section I introduces the sample growth by molecular beam epitaxy. Section II, III and IV give details about transmission electron microscopy, X-ray diffraction and THz measurements, respectively. Section V describes the numerical methods used for DFT calculations. Finally, section VI describes the model for calculating the SCC efficiency., .
- [29] E. E. Pallecchi, F. Lafont, V. Cavaliere, F. Schopfer, D. Maily, W. Poirier, and A. Ouerghi, High electron mobility in epitaxial graphene on 4h-SiC(0001) via post-growth annealing under hydrogen, *Scientific Reports* **4**, 4558 (2014).
- [30] C. Bigi, P. K. Das, D. Benedetti, F. Salvador, D. Krizmancic, R. Sergo, A. Martin, G. Panacione, G. Rossi, J. Fujii, and I. Vobornik, Very efficient spin polarization analysis (VESPA): new exchange scattering-based setup for spin-resolved ARPES at APE-NFFA beamline at Elettra, *Journal of Synchrotron Radiation* **24**, 750 (2017).

- [31] L. Xiang, Y. Ke, and Q. Zhang, Tunable giant Rashba-type spin splitting in PtSe₂/MoSe₂ heterostructure, *Applied Physics Letters* **115**, 203501 (2019).
- [32] A. Ohtomo and H. Y. Hwang, A high-mobility electron gas at the LaAlO₃/SrTiO₃ heterointerface, *Nature* **427**, 423 (2004).
- [33] E. Rongione, L. Baringthon, D. She, G. Patriarche, R. Lebrun, A. Lemaître, M. Morassi, N. Reyren, M. Mićica, J. Mangeney, J. Tignon, F. Bertran, S. Dhillon, P. Le Fèvre, H. Jaffrès, and J.-M. George, Spin-momentum locking and ultrafast spin-charge conversion in ultrathin epitaxial Bi_{1-x}Sb_x topological insulator, *Advanced Science* **10**, 2301124 (2023).
- [34] A. R. Khan, L. Zhang, K. Ishfaq, A. Ikram, T. Yildirim, B. Liu, S. Rahman, and Y. Lu, Optical harmonic generation in 2d materials, *Advanced Functional Materials* **32**, 2105259.
- [35] P. E. Blöchl, Projector augmented-wave method, *Phys. Rev. B* **50**, 17953 (1994).
- [36] G. Kresse and J. Hafner, Ab initio molecular dynamics for liquid metals, *Phys. Rev. B* **47**, 558 (1993).
- [37] G. Kresse and J. Furthmüller, Efficient iterative schemes for ab initio total-energy calculations using a plane-wave basis set, *Phys. Rev. B* **54**, 11169 (1996).
- [38] G. Kresse and J. Furthmüller, Efficiency of ab-initio total energy calculations for metals and semiconductors using a plane-wave basis set, *Computational Materials Science* **6**, 15 (1996).
- [39] J. P. Perdew, K. Burke, and M. Ernzerhof, Generalized gradient approximation made simple, *Phys. Rev. Lett.* **77**, 3865 (1996).
- [40] T. Bučko, J. Hafner, S. Lebègue, and J. G. Ángyán, Improved description of the structure of molecular and layered crystals: Ab initio dft calculations with van der waals corrections, *The Journal of Physical Chemistry A* **114**, 11814 (2010).
- [41] L. Xiang, Y. Ke, and Q. Zhang, Tunable giant rashba-type spin splitting in ptse2/mose2 heterostructure, *Applied Physics Letters* **115**, 203501 (2019).
- [42] D. C. Vaz, P. Noël, A. Johansson, B. Göbel, F. Y. Bruno, G. Singh, S. McKeown-Walker, F. Trier, L. M. Vicente-Arche, A. Sander, S. Valencia, P. Bruneel, M. Vivek, M. Gabay, N. Bergeal, F. Baumberger, H. Okuno, A. Barthélémy, A. Fert, L. Vila, I. Mertig, J.-P. Attané, and M. Bibes, Mapping spin-charge conversion to the band structure in a topological oxide two-dimensional electron gas, *Nature Materials* **18**, 1187 (2019).

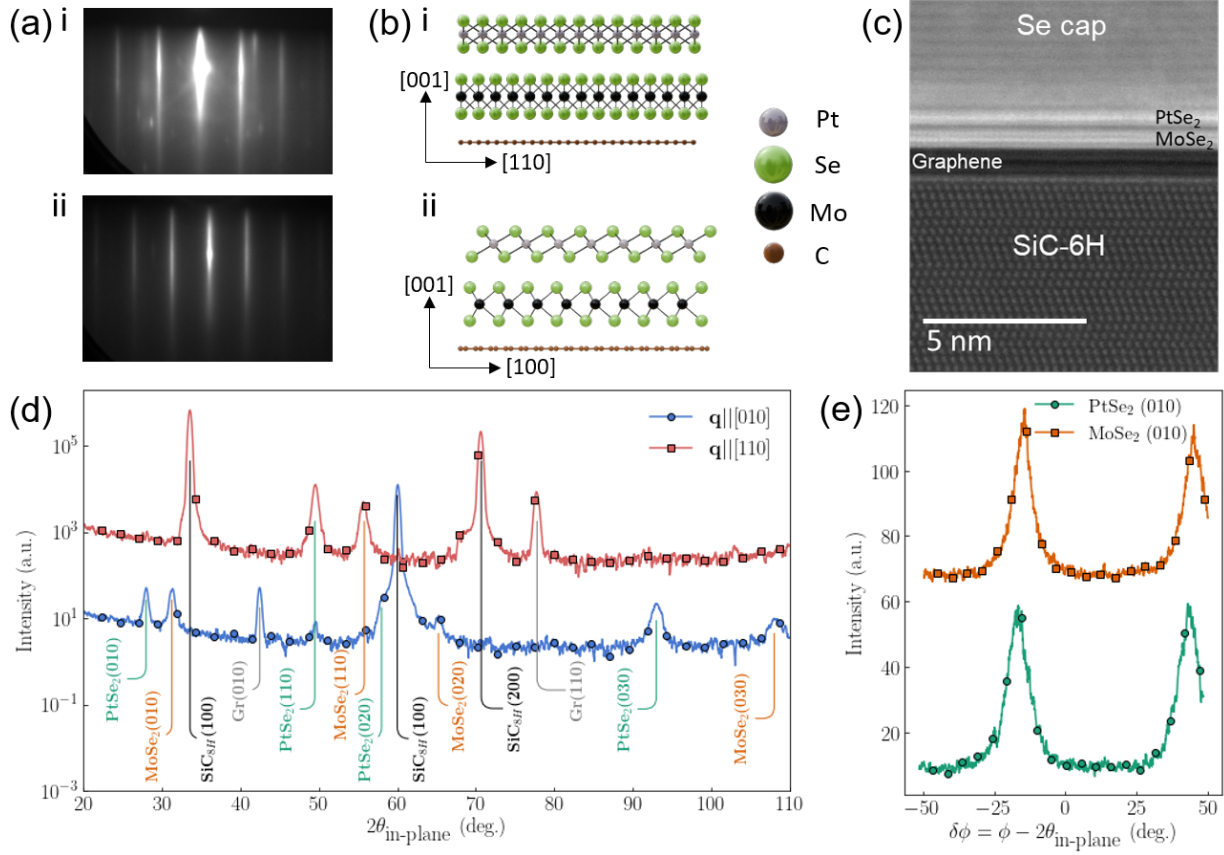


FIG. 1: Growth and characterization of the PtSe₂/MoSe₂/Gr bilayer. (a) RHEED images of (i) MoSe₂ monolayer and (ii) PtSe₂ monolayer along [100]. (b) Atomic model of the layers viewed from the (i) [100] and (ii) [110] directions. (c) Transmission electron microscopy image in cross section of the vdW heterostructure capped with amorphous Se. (d) In-plane radial x-ray diffraction measurements with the momentum transfer \mathbf{q} parallel to the [010] (blue line and circles) and [110] (red line and squares) directions. (e) In-plane azimuthal x-ray diffraction of the PtSe₂ (010) peak (green line and circles) and MoSe₂ (010) peak (orange line and squares).

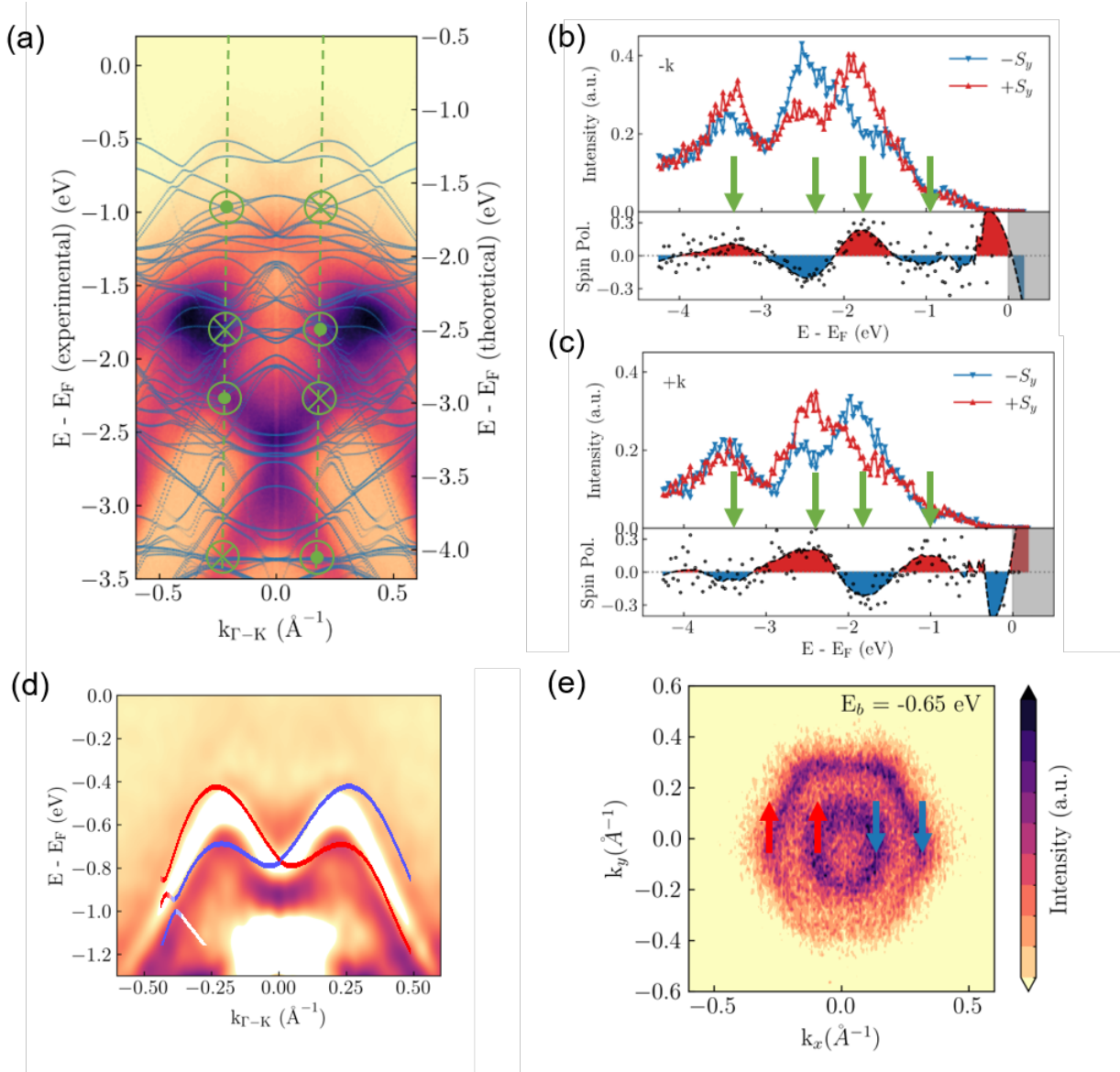


FIG. 2: spin-ARPES of the PtSe₂/MoSe₂/Gr heterostructure. (a) Energy sweep along the Γ -K direction (left axis) with overlaid band structure calculated by DFT (blue, right axis). Spin-resolved energy distribution curves (s-EDCs) at (b) -0.23 \AA^{-1} and (c) $+0.23 \text{ \AA}^{-1}$ corresponding to the vertical dashed lines in (a). Spin textures are reported in (a) according to the spin polarization along y in (b) and (c) at specific energies indicated by vertical green arrows. (d) Second derivative of the raw Spin-ARPES data highlighting the spin-splitting of the sombrero band. The band positions correspond to the dark areas (negative value) on both sides of the bright one (positive value). The red (resp. blue) line corresponds to the calculated band with spin pointing along $+\hat{y}$ (resp. $-\hat{y}$). (e) Constant-energy map in the hybridized sombrero band along with the calculated spin texture at $E_b = -0.65 \text{ eV}$.

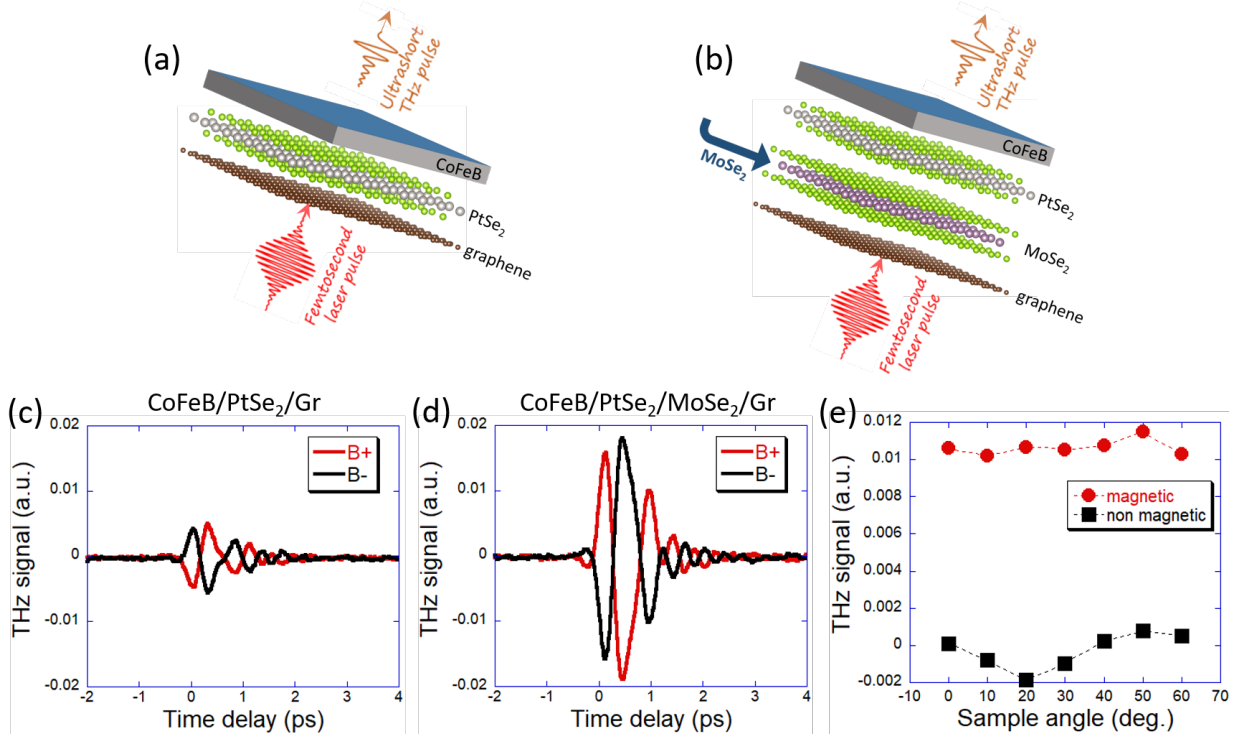


FIG. 3: THz emission results. (a) and (b), schematic of femtosecond optical pumping and THz pulse emission for 1 ML PtSe₂/Gr and bilayer PtSe₂/MoSe₂/Gr systems, respectively. (c) and (d) THz electric field as a function of time delay and magnetic field direction for PtSe₂/Gr and PtSe₂/MoSe₂/Gr systems, respectively. The external magnetic field (strong enough to saturate the CoFeB magnetization) is applied along an azimuthal angle of 0° (red) and 180° (black). (e) Angular dependence of the magnetic S_M and non-magnetic S_{NM} contributions for a fixed magnetic field direction to the emitted THz electric field for PtSe₂/MoSe₂/Gr.

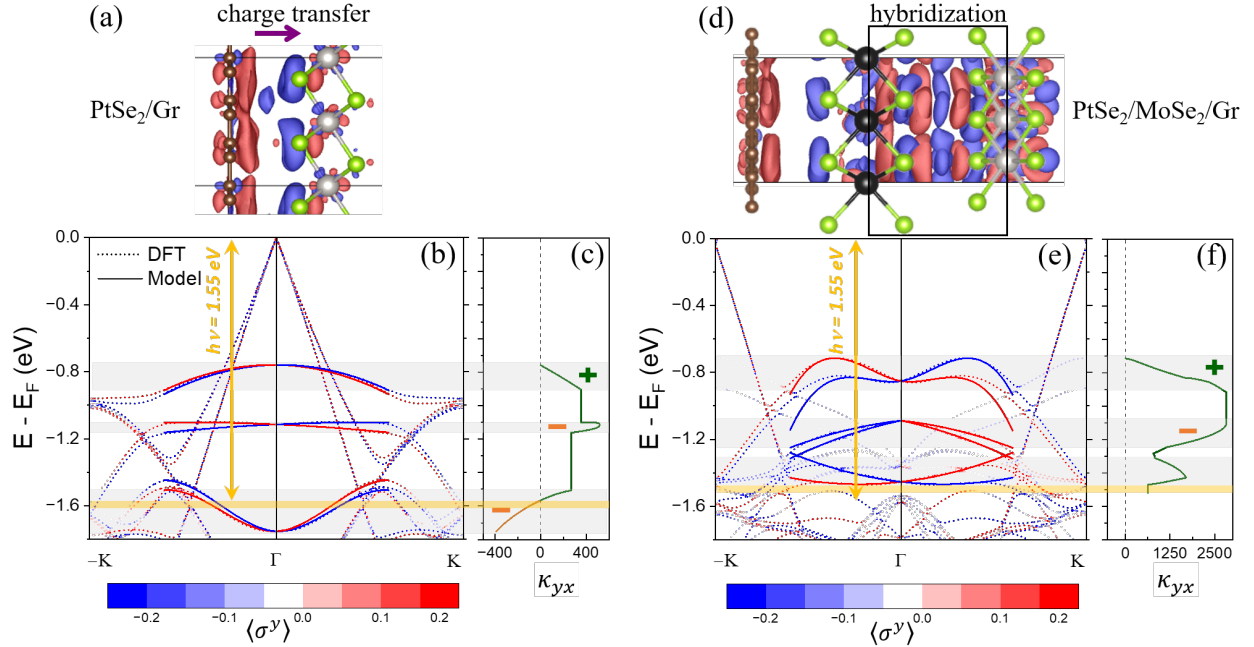


FIG. 4: Crystal structure and calculated charge density in PtSe₂/Gr (a) and PtSe₂/MoSe₂/Gr (d) heterostructures. Blue (red) clouds represent accumulation (depletion) of electrons respectively using an isosurface of $10^{-4} e/\text{\AA}^3$. The interaction mechanism in PtSe₂/Gr is mainly charge transfer whereas the overlap of charge clouds points toward a strong hybridization between PtSe₂ and MoSe₂. The band structure with spin projections along y -direction $\langle\sigma^y\rangle$ are shown for PtSe₂/Gr (b) and PtSe₂/MoSe₂/Gr (e). The dotted lines are the DFT calculated bands whereas the solid lines are the fitted ones using the free-electron model described in the text. The SCC efficiency is quantified by the calculated κ_{yx} tensor in arbitrary units where its cumulative profile is displayed for PtSe₂/Gr (c) and PtSe₂/MoSe₂/Gr (f). The negative sign corresponds to the SCC sign of Co/Pt.